6

Stoichiometry in Inter-Metallic Compounds for Hydrogen Storage Applications

Kwo Young
Ovonic Battery Company, Rochester Hills, Michigan, USA

1. Introduction

This chapter is devoted to the discussion of the influence of stoichiometry deviation on the structure, gaseous phase hydrogen storage, and electrochemical properties of some important inter-metallic compounds (IMC). First, the hydrogen storage characteristics and other important features of the IMC will be reviewed and then there will be a discussion of the AB_5, AB_2, A_2B_7, and AB metal hydride (MH) alloy systems with variations in stoichiometry. The experiments that provide the basis for this chapter's discussion are described in detail (experimental set-up and chosen parameters) in earlier publications (Young, et al., 2008, 2009a, 2010a).

The formation of an IMC between two metallic elements with a fixed stoichiometry depends on the heat of formation of the alloy (ΔH_a). With a very positive value of ΔH_a, the two metallic elements in the alloy are immiscible in the liquid and will stay separate during cooling. As the ΔH_a value decreases but is still positive, a eutectic reaction occurs during cooling, and mixtures of each element with limited solubility of the other is formed. As ΔH_a further decreases to a negative value, a solid solution with a broad range of composition between the two elements is expected. Finally, when ΔH_a becomes very negative, an IMC with a fixed stoichiometry is obtained. Based on the experimental data, ΔH_a of an IMC can be predicted from the electron density at the boundary of the Wigner-Seitz atomic cell and the chemical potential of the conducting electrons (De Boer, et al.,1988). Therefore, the stability of an IMC with a stoichiometry of A_mB_n can be calculated theoretically. Among the choices of crystal structures available to certain stoichiometries of an IMC, the one that minimizes the total electron energy dominates. Parameters such as average electron density, atomic radius ratio, stoichiometry, and difference in electronegativity all contribute to the determination of crystal structure.

In contrast to solid solution, the constituent elements for binary IMC usually have large differences in both size and electronegativity. When the electron transfer takes place, the size of the atoms will change toward the ideal ratio. In the case of IMC, the electron being transferred from the element with the lower electronegativity (usually the larger one) to the other element causes the atomic volume to shrink (Pauling, 1987). This charge transfer changes the local electron density and is very important for the storage of hydrogen.

IMCs can have either a limited or a broad range in stoichiometry (defined as the ratio between constituent elements). For example, all the IMCs in the La-Ni binary phase diagram (Fig. 1) exist at vertical lines, or in other words, there is a unique value of the stoichiometry (ratio between Ni and La) for each IMC; in contrast, the IMCs $ZrNi_5$, $ZrNi_3$, and Zr_7Ni_{10} in the Zr-Ni binary phase diagram (Fig. 2) exist at ranges of composition. The line width (also called solubility for a particular IMC) can be traced to the formation of defects and lattice-adjusted contraction (Thoma & Perepezko, 1995). When there are more A atoms present in the IMC, part of the excessive A atoms either move to B-site (anti-site defect) or create vacancy in B-site (vacancy defect) while still maintaining the same crystal structure. Although the radii ratio between A atom and B atom (R_A/R_B) might not be optimum for the structure, the A-B distance will be adjusted by the defect formation and result in a close-to-ideal lattice. For example, the Laves phase IMC $TiCr_2$ with a less than the ideal ratio of 1.225 (ideal is $\sqrt{1.5}$) has a larger solubility on the A-rich side of the AB_2 stoichiometry (Chen, et al., 1994).

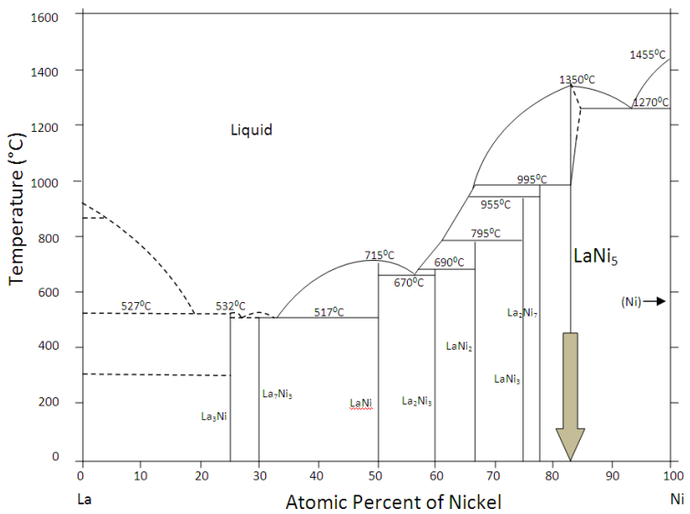

Fig. 1. La-Ni binary phase diagram (data from (Massalski, 1990)).

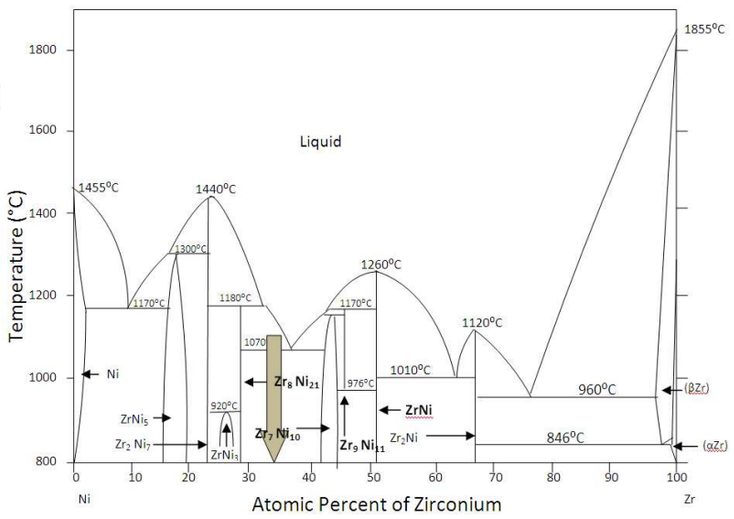

Fig. 2. Ni-Zr binary phase diagram (data from (Massalski, 1990)).

2. Metal hydride alloys

Three different types of chemical bonds can be formed between hydrogen and other elements: the ionic bond, the metallic bond, and the covalent bond for elements with small (Li, Na, for example), medium (Ti, V), and large (N, O) electronegativities, respectively. While the strengths of both ionic and covalent bonds are too large for them to be appropriate for reversible hydrogen storage, the strength of metallic bond can be adjusted for the purpose of hydrogen storage depending on the operation temperature of the application. One way to quantify the metal-hydrogen (M-H) bond strength is by evaluating the heat of hydride formation (ΔH). An application for room temperature, the rechargeable battery for example, would require a ΔH value of between −35 to −30 kJ mol^{-1} H_2. Only expensive metals, such as Pd and V, have the suitable M-H bond strength for room temperature applications. Therefore, the search for hydrogen storage metals was expanded firstly to binary IMCs, such as Mg_2Ni, $LaNi_5$, and TiNi, and then to more complicated and multi-element IMCs.

When hydrogen enters into the bulk of the metal, it contributes its only electron to the conduction band. The remaining proton then goes into the interstitial site among four or six host elements, causing an expansion in the crystal lattice. The metal hydride formed this way, shown in Fig. 3, has the same or very similar crystal structure as the host metal. Driven by a concentration gradient, the proton jumps to the neighboring storage sites through quantum mechanical tunneling. The moving path of the proton in AB_2 C14 MH alloy is along the vertical (*c*-) axis (Fig. 3a), which is different from its movement on the horizontal (*a*-*b*) plane in AB_5 MH alloy (Fig. 3b). Therefore, a flattened and an elongated unit cell along the *c*-axis are preferable for the ease of proton movement in AB_2 and AB_5 metal hydride (MH) alloys, respectively (Osumi, et al., 1983, Young, et al., 2009b).

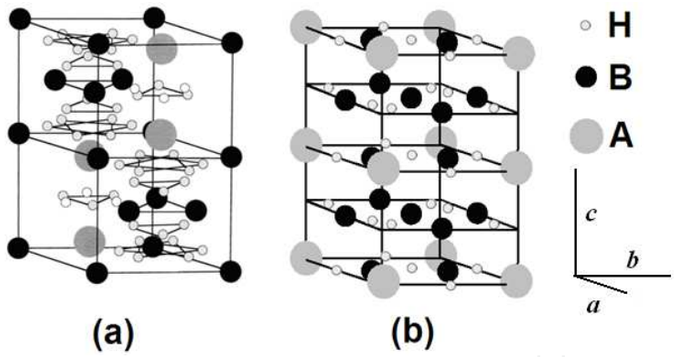

Fig. 3. Crystal structures of C14-AB_2H_4 (a) and AB_5H_6 (b) MH alloys.

The process of hydride formation can be described by the pressure-concentration-temperature (PCT) curves shown in Fig. 4, where the logarithm of the equilibrium hydrogen pressure is plotted against the hydrogen concentration in metal. At a fixed temperature, when the concentration of hydrogen in the bulk is low, the protons are randomly distributed throughout the host metal (α-phase). As the applied hydrogen pressure increases, more hydrogen atoms enter into the metal and start to form MH clusters, similarly to the beginning of ice formation in the case of freezing water. The co-existence of metal (α-phase) and MH (β-phase) eliminates the freedom in pressure and thus contributes to the flat region

(plateau) of the PCT curve. With further increase in hydrogen pressure, the transformation into β-phase is complete, marks the end of the pressure plateau, and isotherm becomes more vertical. The The PCT curves can be measured with stepwise increases (absorption) or decreases (desorption) in applied hydrogen pressure. These two curves do not align with each other, and the difference in the plateau pressures of the two curves is called the hysteresis of PCT curve. The hysteresis represents the resistance of the metal against the pushing in or pulling out of additional hydrogen atoms. The correlation between the hysteresis and the MH pulverization rate through hydride/dehydride cycles is well established: MH alloys with small hysteresis are less prone to break into small pieces during cycling. Each set of the PCT curves (absorption and desorption) is obtained at one particular temperature. As the temperature increases, $T_3 > T_2 > T_1$ in Fig. 4, the following occur: the regions of α- and β-phases extend into the plateau region due to the higher entropy in the system, the plateau region shortens, the plateau pressure increases, and hysteresis, reversible and maximum hydrogen storage capacities reduce. By connecting all the boundary points between α-phase, $\alpha + \beta$ mixed phase, and β-phase, a dome-shaped curve is obtained. As the temperature rises above a certain critical value (T_3 in Fig. 4), the plateau region of the PCT curve completely disappears. This critical temperature is very material-dependent. In the case of $LaNi_5$ based MH alloys, the systems are very ordered, and the critical temperatures are very high. Therefore, most of the PCT curves observed around room temperature are very flat. On the other hand, the multi-phase (Ti, Zr)Ni_2 based MH alloys have lower critical temperatures due to their high degrees of disorder inherent with the alloys and produce PCT curves without recognizable plateau region. Slope factor, defined as the percentage of storage capacity within a pressure range (usually from 0.01 to 0.5 MPa), is used to quantify the slope of the PCT isotherm.

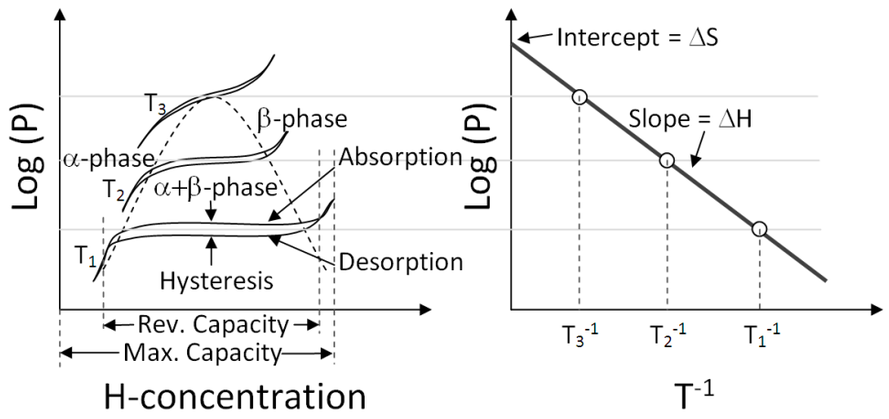

Fig. 4. Schematics of PCT isotherm (left) and the corresponding Van't Hoff diagram (right).

The plateau pressures in the PCT curves can be used to calculate the changes in enthalpy (ΔH) and entropy (ΔS) by the equation

$$\Delta G = \Delta H - T\Delta S = RT \ln P \quad (1)$$

where R is the ideal gas constant and T is the absolute temperature. When the logarithm of the pressure is plotted against the reciprocal of the absolute temperature as shown in Fig. 4,

ΔH and ΔS can be calculated from the slope and the y-axis intercept of the line, respectively. The value of ΔH can be used to quantify the M-H bond strength. MH with a lower ΔH (more negative) will release more heat during the formation of a more stable hydride with a lower equilibrium pressure, indicating both a stronger M-H bond and a larger interstitial site for hydrogen. For an ordered MH, ΔS is around the standard entropy of hydrogen gas (−130 J K^{-1} mol^{-1} H_2). ΔS will be higher for a less ordered MH.

Besides the application of solid hydrogen storage, MH alloys also play a very important role in nickel/metal hydride (Ni/MH) rechargeable battery as the negative electrode. The chemical reaction during charge/discharge is:

$$M + Ni(OH)_2 \underset{\text{discgarge}}{\overset{\text{charge}}{\rightleftharpoons}} MH + NiOOH \quad (2)$$

During charge, the water molecule near the surface of the MH electrode splits into a proton (H^+) and a hydroxide ion (OH^-) by the applied voltage. While OH^- moves into the electrolyte, H^+ enters into the bulk of the MH and is neutralized by the electron coming from the current collector. Charging/discharging in the electrochemical environment is very similar to hydriding/dehydriding in the gaseous phase; these two reactions can be linked by the Nernst Equation:

$$\text{Open circuit voltage vs. Hg/HgO} = -0.934 - 0.0291 \log P_{H2} \quad (3)$$

where Hg/HgO is the reference electrode commonly used in alkaline solution. This correlation explains the similarity between the PCT curves (Fig. 4) and the electrochemical charge/discharge curves illustrated in Fig. 5. The origin for the voltage difference between charge and discharge curves is quite complicated and contains at least the ohmic resistance in the connector and substrate, resistance from surface reaction, limited hydrogen diffusion, and electrolyte concentration difference. At a higher rate (gray curves in Fig. 5), the charge voltage is higher while the discharge voltage and the obtained capacity are lower, mostly due to the increase in current (i) as

$$V = OCV + iR \text{ (during charge) and} \quad (4)$$

$$V = OCV - iR \text{ (during discharge)} \quad (5)$$

where OCV is the open circuit voltage and R is the internal resistance.

Currently, there are four main MH alloy families used or proposed to be used as the negative electrode for Ni/MH rechargeable battery: the AB_5, AB_2, A_2B_7 and AB alloy families. Rare earth element-based AB_5 alloy family is the most commonly used, with the misch-metal (Mm) (mixture of light rare earth elements, such as La, Ce, Nd, and Pr) as the A-elements and Ni, Mn, Al, and Co as the B-elements. Ni is an indispensably key element in alkaline electrochemistry due to its corrosion resistance and catalytic nature for water splitting/recombination. Other modifiers all have different contributions. The main advantages of AB_5 MH alloy are its high power capability as a result of the high Ni-content and superior cycle life. The transition metal-based AB_2 alloy (with Zr and Ti as the A-elements and B-elements similar to those of the AB_5 alloy) offers a reduction in raw material cost due to

the elimination of rare earth elements and also has the advantage in storage capacity. In A_2B_7 MH alloy, a small amount of Mg is added to the mixture of A-elements (which is composed of rare earth elements) to stabilize the crystal structure. The special super-lattice structure of A_2B_7 MH alloy provides a compromise in performance between AB_2 and AB_5. The last alloy family for Ni/MH application is the Mg-Ni based AB alloy. The much weaker M-H bond of Mg when compared to other A-elements, such as La, Ce, Zr, and Ti, reduces the desirable stoichiometry down to 1:1. The abundance of the raw material and high storage capacity of AB alloy make it a potential candidate to further reduce cost and improve capacity. The impact of stoichiometry on the structures, gaseous phase hydrogen storage properties, and electrochemical properties for these four alloy families will be presented in the remaining sections.

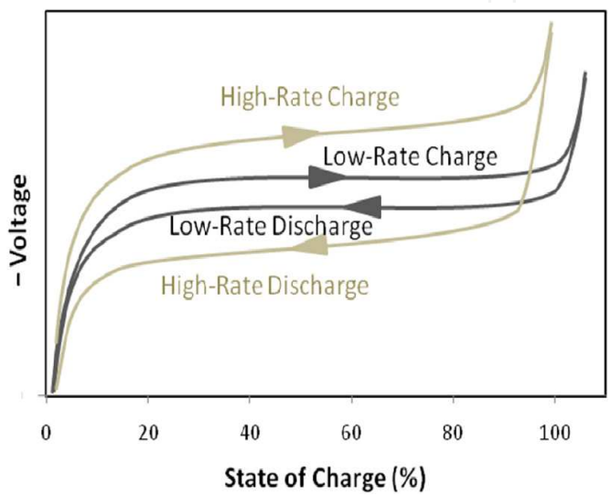

Fig. 5. Schematics of charge and discharge curves under a high (gray) and a low (black) charge densities

3. Stoichiometry in $LaNi_5$-based metal hydride alloys

According to the phase diagram (Fig. 1), eight IMCs exist in the La-Ni binary system. As the Ni-content increases, the ΔH of the hydride increases and forms a straight line in Fig. 6. Since the operational conditions for Ni/MH battery are room temperature and 1 atm, the suitable ΔH value for the MH alloy is around −40 kJ mol^{-1} H_2 (by assigning ΔS to the average value of −130 J K^{-1} mol^{-1} H_2 in formula (1)). In the IMCs of La and Ni, only ΔH of $LaNi_5$ falls into the range suitable for room temperature Ni/MH application. As a result, $LaNi_5$-based MH alloy was chosen as the negative electrode in Ni/MH battery from early on and still dominates today's market.

The following is a description of the sample preparation for the experimental work backing this publication. Five Mm-based AB_5 alloys were prepared by arc melting. The composition of ingot prepared by arc melting is not as uniform as the commercial product produced by induction melting. The designed compositions of these alloys are listed in Table 1 with increasing B/A stoichiometric ratios from 4.8 (hypo) to 5.2 (hyper). The base alloy, AB5.0, is commonly used in today's high-power Ni/MH rechargeable battery and achieves a good balance among different performances. The ingots were annealed in vacuum (1×10^{-8} torr) at 960°C for 8 hours before being mechanically crushed into −200 mesh powder

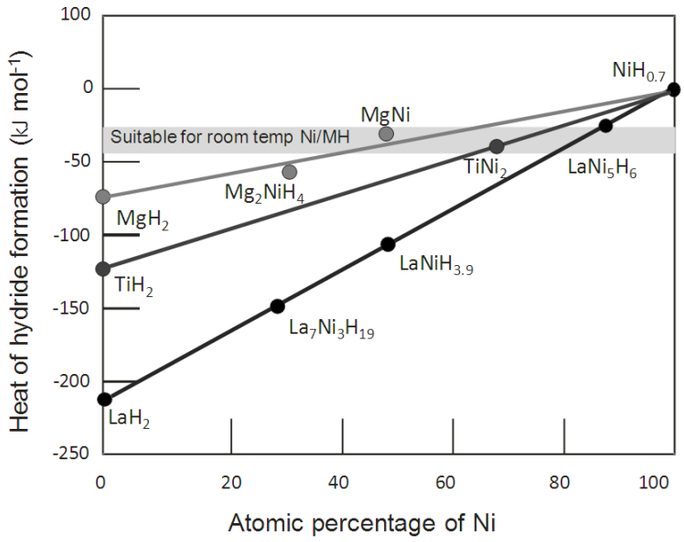

Fig. 6. Relationship between heat of hydride formation and atomic percentage of Ni in the alloy for AB (MgNi), AB_2 ($TiNi_2$), and AB_5 ($LaNi_5$) inter-metallic compounds.

Alloy	La	Ce	Pr	Nd	Ni	Co	Mn	Al	B/A
AB4.8	10.9	4.5	0.5	1.5	59.6	12.6	5.9	4.7	4.8
AB4.9	10.7	4.4	0.5	1.4	59.8	12.7	5.9	4.7	4.9
AB5.0	10.5	4.3	0.5	1.4	60.0	12.7	5.9	4.7	5.0
AB5.1	10.3	4.2	0.5	1.4	60.2	12.7	5.9	4.7	5.1
AB5.2	10.2	4.2	0.5	1.4	60.4	12.8	5.9	4.7	5.2

Table 1. Designed compositions in at. % and B/A stoichiometry ratios of AB_5 alloys.

3.1 Influences on microstructure

In Fig. 1, $LaNi_5$ is represented by a straight line in the phase diagram and shows no solubility at room temperature. If the liquid is quenched very quickly, some hyper-stoichiometry is possible, as can be seen from the dash line near 1270°C; however, annealing and slow cooling will eliminate this hyper-stoichiometry. After annealing, a La_2Ni_7 and a Ni phase are expected in the cases of hypo- and hyper-stoichiometries, respectively. In a commercial AB_5 alloy suitable for general performance requirements, A is mainly Mm (combination of La, Ce, Pr, and Nd) while B contains Ni, Co, Mn, and Al. The multi-element nature of the alloy system will increase the solubility of particular phases since anti-site or vacancy defects become easier to form in multi-element systems.

The phases of the five AB_5 alloys were first studied by x-ray diffractometer (XRD); the results are presented in Fig. 7. Almost all peaks can be attributed to a $CaCu_5$ structure. Ni peak starts to appear when the stoichiometry becomes ≥ 5.0. The lattice parameters and ratio, unit cell volume, and phase abundances obtained from XRD for each alloy are listed in Table 2. As the B/A stoichiometric ratio increases from 4.8 to 5.2, both *a* and *c* lattice

constants first increase and then decrease. The maximums occur at a B/A stoichiometric ratio of 4.9, where the *c*/*a* ratio reaches the minimum, suggesting a higher pulverization rate during hydride/dehydride cycling. The Ni phase abundance increases with the increase in B/A stoichiometric ratio.

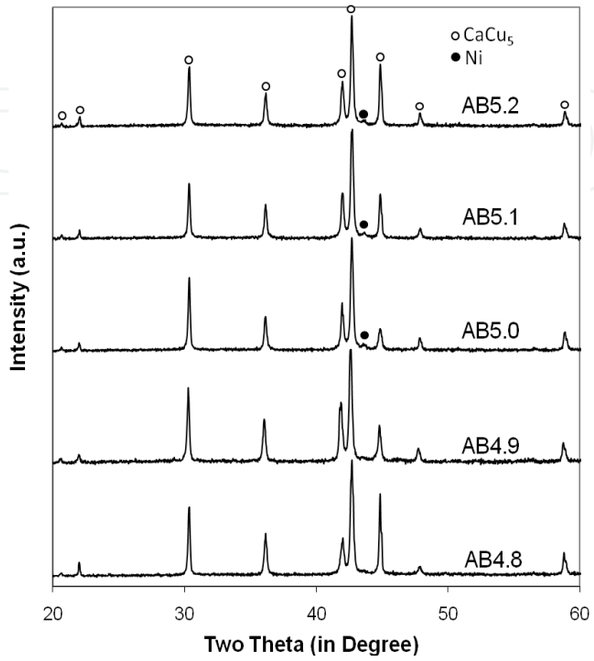

Fig. 7. XRD patterns of AB_5 alloys using Cu-K_α as the radiation source.

Alloy	*a* (Å)	*c* (Å)	*c*/*a*	Unit cell volume (Å^3)	$CaCu_5$ %	Ni %
AB4.8	4.984	4.052	0.813	87.17	100.0	ND
AB4.9	5.002	4.055	0.811	87.86	100.0	ND
AB5.0	4.986	4.052	0.813	87.23	99.6	0.4
AB5.1	4.984	4.051	0.813	87.14	99.4	0.6
AB5.2	4.985	4.051	0.813	87.18	99.2	0.8

Table 2. Lattice constants and ratios, unit cell volumes, and phase abundances of $CaCu_5$ and Ni of AB_5 alloys from XRD analysis.

The microstructures were further studied by scanning electron microscope (SEM); the resulting backscattering electron images (BEI) are shown in Fig. 8. These micrographs were chosen due to the presence of multi-phase features and do not represent the general phase distribution of the alloys. Four distinctive phases, *A*, *B*, *C*, and *D*, can be identified from these micrographs. Phase *A*, with the brightest contrast due to its high average atomic weight, is the misch-metal with the composition very close to the raw material as indicated by x-ray energy dispersive spectroscopy (EDS) analysis. Phase *B* has a composition close to AB, which is the phase on the left-hand side of the eutectic point in Fig. 1. The AB phase

abundance is too small to be detected by XRD analysis. Phase *C* is the main AB_5 phase, where the B/A stoichiometric ratio increases from 5.17, 5.29, 5.49, 5.48, finally to 5.47 with the increase in designed B/A values. In other words, the solubility of the AB_5 phase extends to about 5.5 in this case as the alloy's B/A stoichiometric ratio increases. Further increase of the B-content in the alloy promotes the formation of Ni-phase as seen from Fig.1 and Table 2. Phase *D* with the darkest contrast is a mixture of transition metals and has an average composition of $Al_9Mn_{21}Co_{20}Ni_{50}$, which is high in Al and Mn and low in Ni when compared to the raw material.

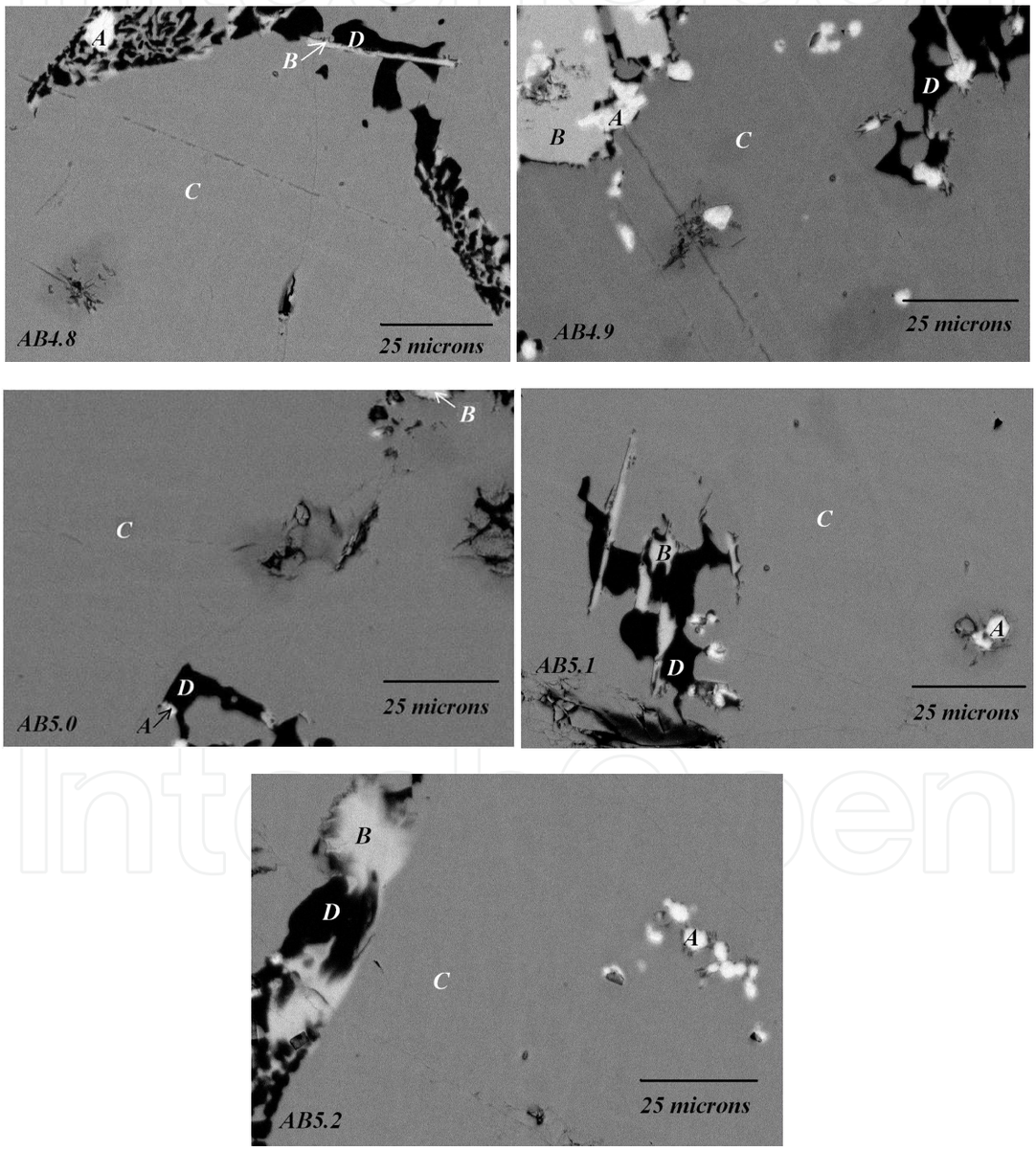

Fig. 8. SEM backscattering images for AB5 alloys. Letters A, B, C, and D indicate metallic rare earth elements, LaNi, $LaNi_5$, and transition metals, respectively.

3.2 Influences on gaseous hydrogen storage

The gaseous phase hydrogen storage characteristics were studied by PCT measurements performed at 30 and 60°C. The 30°C PCT isotherms from the five AB_5 alloys are plotted in Fig. 9 and summarized in Table 3. As the designed B/A stoichiometric ratio increases, both the maximum and reversible hydrogen storage capacities measured at 30°C first increase and then decrease. This trend is the same as that in unit cell volume. The larger unit cell contributes to a more stable hydride with lower equilibrium pressure and higher storage capacity. The isotherm from AB4.9 is flatter than those from other alloys, indicating a higher uniformity in the main phase. The PCT hysteresis from AB4.9 is the highest and corresponds to its lowest c/a ratio among all alloys, suggesting a more difficult tunneling path for protons to hop within the structure. ΔH and ΔS were calculated from the plateau pressures measured at 30 and 60°C by formula (1) and are listed in Table 3. ΔH and ΔS values are about the same.

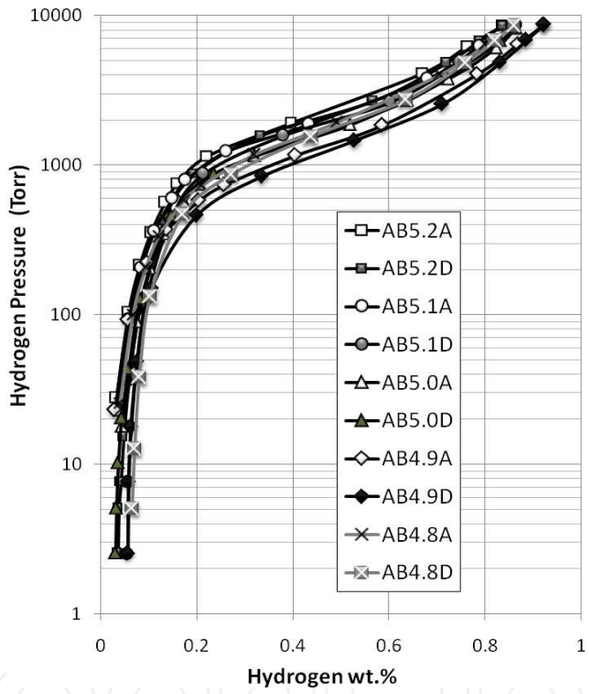

Fig. 9. PCT isotherms measured at 30°C for AB_5 alloys. Open and solid symbols represent data taken during absorption and desorption, respectively.

Alloy	Max. H-storageat 30°C (wt. %)	Reversible H-storageat 30°C wt. %)	Plateau pressure at 30°C Des. (torr)	30°C slope factor	30°C hysteresis	$-\Delta H$ (kJ mol^{-1} H_2)	$-\Delta S$ (J K^{-1} mol^{-1} H_2)
AB4.8	0.86	0.80	1683	0.76	0.06	30	104
AB4.9	0.92	0.86	1479	0.87	0.10	30	105
AB5.0	0.86	0.83	1555	0.80	0.01	30	105
AB5.1	0.86	0.80	1944	0.75	0.06	29	105
AB5.2	0.84	0.80	2068	0.72	0.08	30	106

Table 3. Summary of gaseous phase hydrogen storage properties of AB_5 alloys.

3.3 Influences on electrochemical properties

The discharge capacities for the five AB_5 alloys were measured at two discharge current densities (100 and 8 mA g^{-1}), and the results are listed in Table 4. The full capacity, defined as the capacity measured at the slowest discharge rate (8 mA g^{-1}), increases first and then decreases with the increase in B/A stoichiometric ratio. The stoichiometric AB5.0 alloy shows the highest capacity. The high-rate dischargeability (HRD) values (ratios between the capacities measured at 100 and 8 mA/g discharge currents) measured at the third cycle are listed in Table 4. The maximum HRD value was obtained from a slightly hyper-stoichiometric AB5.1 alloy.

Alloy	Full capacity (mAh g^{-1})	High-rate capacity (mAh g^{-1})	Ratio (High-rate dischargeability)	OCV at 50% DOD (V)
AB4.8	216	203	0.94	−0.921
AB4.9	246	233	0.95	−0.914
AB5.0	249	237	0.95	−0.922
AB5.1	214	205	0.96	−0.927
AB5.2	215	200	0.93	−0.931

Table 4. Summary of electrochemical properties of AB_5 alloys.

OCV measured at 50% depth-of-discharge (DOD) of the MH electrode against the Hg/HgO reference electrode for each alloy is listed in Table 4. In the AB_5 alloy series, the changes in OCV are small due to their similar plateau pressures. In general, OCV decreases with the increase in B/A stoichiometric ratio, which correlates well with the increase in plateau pressure by formula (3). Lower OCV value is a desirable trait because it will contribute to higher cell voltage and better power in the sealed battery configuration.

4. Stoichiometry in Laves phase-based AB_2 metal hydride alloys

Compared to La, Ti has a lower M-H bond strength and thus requires a smaller amount of Ni to adjust the heat of hydride formation to fall within the desired range. According to the graph that plots ΔH vs. atomic percentage of Ni (Fig. 6), a stoichiometry of approximately AB_2 would be suitable for room temperature Ni/MH application. However, the IMC of $TiNi_2$ is not available according to the Ti-Ni binary phase diagram. As seen from the Zr-Ni phase diagram in Fig. 2, Zr, a common element used to partially replace Ti in order to adjust the hydrogen storage, does not have an IMC at $ZrNi_2$ either. Since $TiCr_2$, $ZrCr_2$, $TiMn_2$, and $ZrMn_2$ are all available based on the phase diagrams (Fig. 10, for example), the design of AB_2 alloy starts from the formulation of $(Ti, Zr)(Ni, Cr, Mn)_2$. There are three AB_2 Laves phases, namely, C14, C15, and C36. From the Zr-Cr phase diagram in Fig. 10, the order of phase formation during cooling is C14 first, followed by C36, and finally the C15 phase. Due to the existence of defects, $ZrCr_2$ has a broad range of solubility, allowing the designed composition to be off-stoichiometric.

Five transition element-based AB_2 alloys were prepared by arc melting, and the designed compositions are listed in Table 5. The designed B/A stoichiometric ratio varies from 1.8

(hypo) to 2.2 (hyper). The average electron density (e/a) of each alloy, based on the numbers of outer-shell electrons of the constituent elements, is listed in Table 5 and can be used to predict the dominant phase (C14 or C15) (Shaltiel, et al., 1977). The base alloy, AB2.0, is rich in C14 phase and a candidate for replacing AB_5 alloy in Ni/MH batteries. Its microstructure was studied extensively with a combination of SEM and transmission electron microscope previously (Boettinger, et al., 2010, Bendersky, et al., 2010). In order to preserve the secondary phases, which serve as an electrochemical catalyst, these AB_2 alloys were not annealed (Young, et al., 2010b).

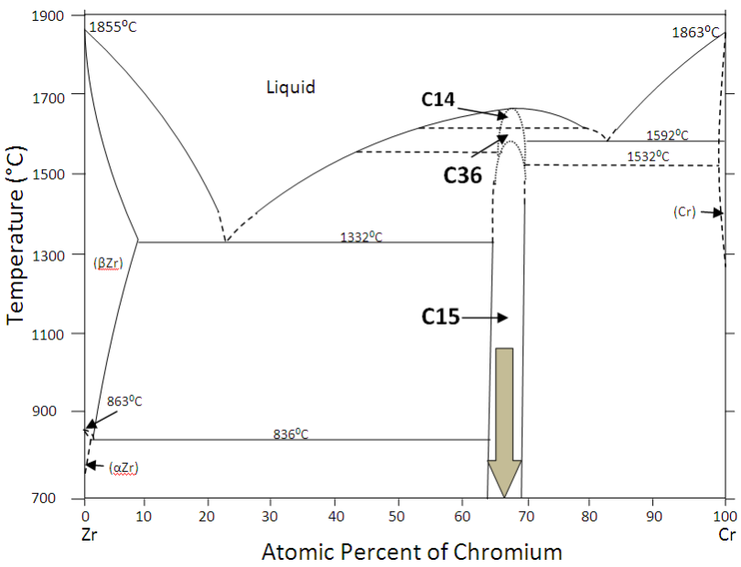

Fig. 10. Zr-Cr binary phase diagram (data from (Massalski, 1990)).

Alloy	Zr	Ti	V	Cr	Mn	Co	Ni	Al	Sn	B/A	e/a
AB1.8	22.4	13.3	9.7	8.2	5.4	1.5	38.9	0.4	0.3	1.8	6.85
AB1.9	21.7	12.9	9.8	8.4	5.5	1.5	39.5	0.4	0.3	1.9	6.90
AB2.0	21.0	12.5	10.0	8.5	5.6	1.5	40.2	0.4	0.3	2.0	6.95
AB2.1	20.2	12.0	10.2	8.7	5.7	1.5	41.0	0.4	0.3	2.1	7.01
AB2.2	19.6	11.7	10.3	8.8	5.8	1.6	41.6	0.4	0.3	2.2	7.05

Table 5. Designed compositions in at. %, B/A stoichiometry ratios, and average electron densities (e/a) of AB_2 alloys.

4.1 Influences on microstructure

Fig. 11 compares the XRD patterns from the five AB_2 alloys. As the e/a value increases, the main phase shifts from C14 to C15. Besides the main Laves phases, TiNi phase, which is associated with the solid-state transformation of non-Laves secondary phases during cooling, is also present. The C14 lattice constants a and c, c/a aspect ratio, unit cell volume, and phase abundances of each alloy are listed in Table 6. In this series of AB_2 alloys, a and c

decrease monotonically with the increase in stoichiometry. In the case of hypo-stoichiometry, the excessive A-site atoms move to the B-site and slightly enlarge the unit cell. On the contrary, the larger B-site elements (however, still smaller than the A-site elements) will occupy the A-site and shrink the unit cell in the case of hyper-stoichiometry (Kodama, et al., 1995). The stoichiometric AB2.0 alloy has the highest or close to the highest c/a aspect ratio, so theoretically it should be the least stable alloy during hydride/dehydride cycling. The C14 unit cell volume decreases with the increase in B/A stoichiometric ratio. The smaller unit cell will contribute to an unstable hydride with higher plateau pressure and lower storage capacity. As the B/A stoichiometric ratio increases, more of the main C14 phase was replaced by the C15 phase due to the increase of the e/a value. The phase abundance of TiNi also reduces with the increase in B/A stoichiometric ratio. The TiNi phase has a higher A-atom content than the Laves phase does and therefore is not favorable in the case of B-rich hyper-stoichiometry.

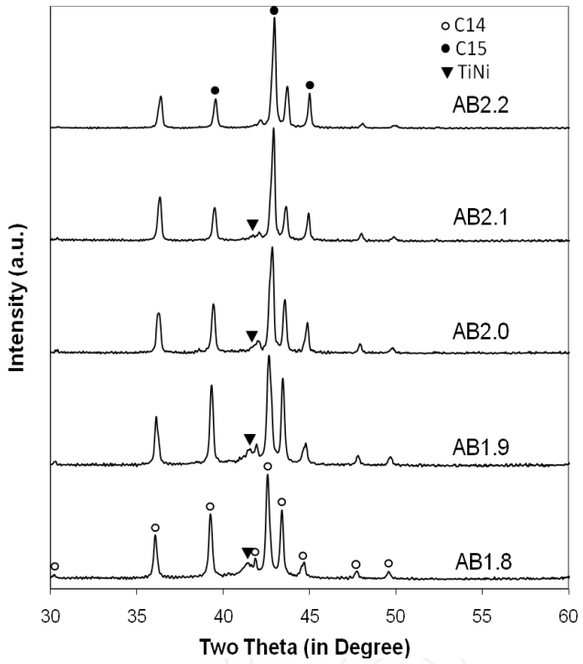

Fig. 11. XRD patterns of AB_2 alloys using Cu-K_α as the radiation source.

Alloy	a (Å)	c(Å)	c/a	Unit cell volume (Å^3)	C14 %	C15 %	TiNi %
AB1.8	4.9932	8.1471	1.632	175.9	74.0	11.1	14.9
AB1.9	4.9831	8.1381	1.633	175.0	74.8	17.0	8.2
AB2.0	4.9771	8.1288	1.633	174.4	70.7	25.7	3.6
AB2.1	4.9634	8.1005	1.632	172.8	62.3	36.7	1.0
AB2.2	4.9564	8.0882	1.631	172.1	60.0	40.0	0.0

Table 6. C14 lattice constants and ratios, unit cell volumes, and phase abundances of C14, C15 and TiNi of AB_2 alloys from XRD analysis.

Four regions with different contrasts can be observed in most of the SEM BEI micrographs shown in Fig. 12. Region *A* with the brightest contrast is the Zr_7Ni_{10} phase, which was not observed in XRD due to its small abundance. The light gray region *B* has a composition close to AB and can be related to the TiNi phase found in XRD analysis. Both regions *A* and *B*, with nominal compositions of A_7B_{10} and AB, become smaller and even diminish as the B/A stoichiometric ratio increases. Region *C* is the main AB_2 phase. As the designed B/A stoichiometric ratio increases, the B/A stoichiometric ratio in the main AB_2 phase evolves from 1.85 to 1.97, 2.05, 2.01 and 1.99. This result demonstrates that the AB_2 phase has a wider solubility on the hypo-side than on the hyper-side in the C14-predominaing case. The last feature of the micrographs is the dark spot with very high Zr-content, which is identified as ZrO_2 inclusion (region *D*). This oxide is formed through oxidation of Zr segregated out from the melt; it is not the residual oxide in the raw material as reported before in a study of ZrO_2 inclusions in the Al-containing AB_2 alloys [Young, et al., 2010c]. As the B/A stoichiometric ratio varies, the size and amount of ZrO_2 inclusions do not change.

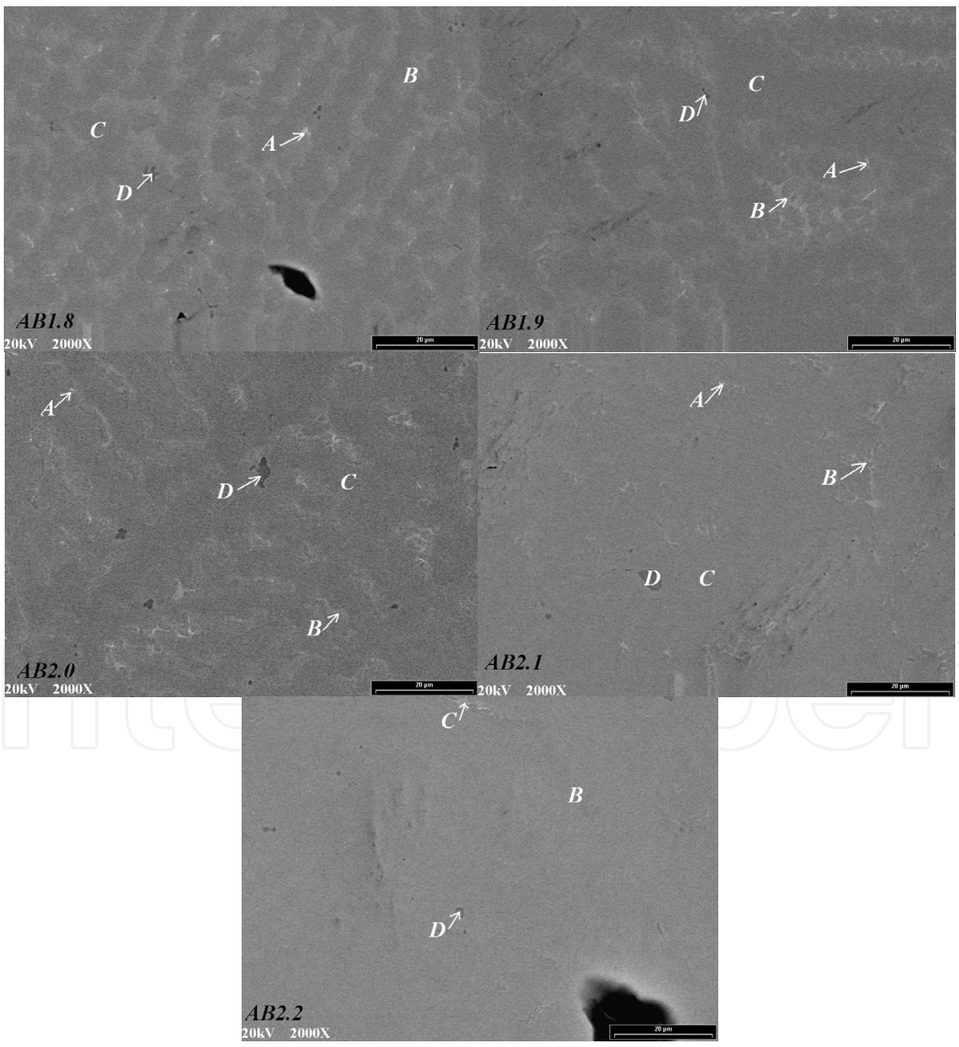

Fig. 12. SEM backscattering images for AB_2 alloys. Letters *A*, *B*, *C*, and *D* indicate Zr_7Ni_{10}, TiNi, AB_2, and ZrO_2, respectively.

4.2 Influences on gaseous hydrogen storage

The PCT absorption and desorption isotherms measured at 30°C for the five AB_2 alloys are plotted in Fig. 13 and summarized in Table 7. As the B/A stoichiometric ratio increases, the maximum hydrogen storage capacity first increases and then decreases. The highest maximum capacity was obtained from AB1.9 alloy. For the alloys with B/A stoichiometric ratio ≥ 2.0, the maximum capacities decrease as a result of the shrinking lattice unit cell. In alloy AB1.8, the phase abundance of C14, which has less storage capacity compared to C15 (Young, et al. 2010b), is the highest and thus decreases the maximum storage capacity. The relationship between B/A stoichiometric ratio and reversible gas phase storage is similar to what is observed in maximum storage capacity: as the B/A stoichiometric ratio first increases, the reversible storage increases due to the higher plateau pressure and the higher C15 phase abundance with higher gaseous reversibility (Young, et al. 2010b). With further increase in B/A stoichiometric ratio, the reversible storage capacity decreases for the same reason as the maximum storage capacity. The maximum reversible capacity happens at AB2.0. Due to the high degree of disorder in AB_2 MH alloys, the critical temperature (top of the dome expressed by a dashed line in Fig. 4) is much lower than it is in AB_5 MH alloys. Therefore, all the PCT isotherms lack a well-defined plateau pressure, or in other words, a metal (α)-hydride (β) co-existing region. In order to compare the hydrogen equilibrium pressures among the alloys, the mid-point pressure, defined as the pressure where half of the desorption is complete, is calculated and listed in Table 7. The mid-point pressure increases as a result of shrinking lattice unit cell as the B/A stoichiometric ratio goes up. With the increase in B/A stoichiometric ratio, the PCT isotherm becomes flatter except the last AB2.2 alloy. Slightly hyper-stoichiometry (2.1) shows the most ordered structure.

Alloy	Max. H-storage at 30°C (wt. %)	Reversible H-storage at 30°C (wt. %)	Mid-point pressure at 30°C Des. (torr)	30°C slope factor	30°C hysteresis	$-\Delta H$(kJ mol^{-1} H_2)	$-\Delta S$ (J K^{-1} mol^{-1} H_2)
AB1.8	1.30	0.78	150	0.59	0.69	29	77
AB1.9	1.44	1.09	200	0.66	0.59	28	81
AB2.0	1.40	1.16	500	0.79	0.09	24	77
AB2.1	1.31	1.13	700	0.81	0.13	23	76
AB2.2	1.11	0.91	1100	0.78	0.25	21	71

Table 7. Summary of gaseous phase hydrogen storage properties of AB_2 alloys.

For AB2.0-stoichiomtery alloys, the hysteresis is related to the average electron density (Young, et al. 2009b). The PCT hysteresis first decreases and then increases with the increase in B/A stoichiometric ratio. The hysteresis minimum happens at a B/A stoichiometric ratio of 2.0. Therefore, from a cycle stability point of view, the stoichiometric AB2.0 alloy is preferable and contradicts from the c/a ratio prediction in the XRD analysis. ΔH and ΔS values, calculated from the mid-point pressures of 30 and 60°C desorption isotherms, are listed in Table 7. The value of $-\Delta H$ decreases as the B/A

stoichiometric ratio decreases, which implies the weakening of the M-H bond strength and correlates well with the shrinking lattice. The measured ΔS values from these AB_2 alloys are similar and higher than those in AB_5 alloys (around −105 J K^{-1} mol^{-1} H_2), which suggest higher degrees of disorder in AB_2 alloys and are consistent with the steeper PCT isotherms.

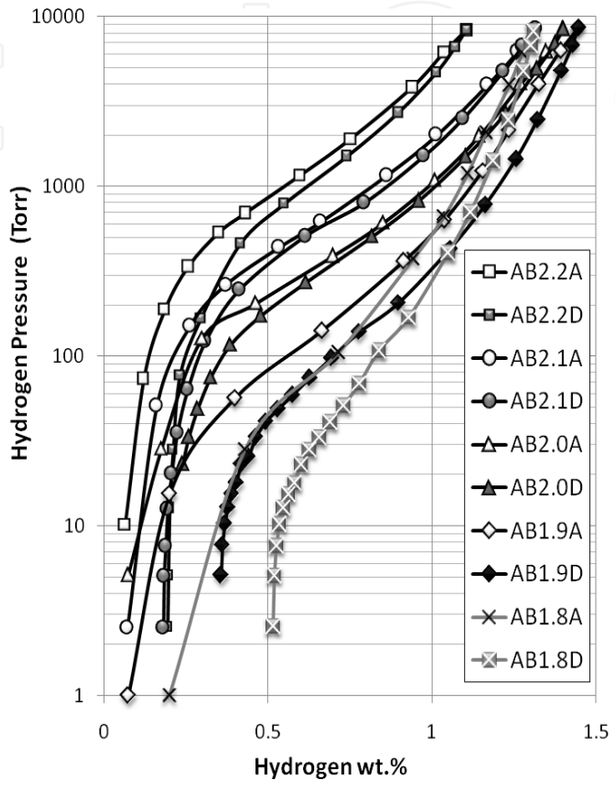

Fig. 13. PCT isotherms measured at 30°C for AB_2 alloys. Open and solid symbols represent data taken during absorption and desorption, respectively.

4.3 Influences on electrochemical properties

The discharge capacities for the five AB_2 alloys were measured, and the results are listed in Table 8. The full capacity increases first and then decreases with the increase in B/A stoichiometric ratio. The stoichiometric AB2.0 alloy shows the highest capacity. The HRD values measured at the tenth cycle are listed in Table 8. The maximum value occurs at AB2.1. Similar to the case of AB_5 alloys, slightly hyper-stoichiometry increases the HRD.

OCV measured at 50% DOD of the MH electrode against Hg/HgO reference electrode for each alloy is listed in Table 8. In the AB_2 alloy series, OCV decreases with the increase in B/A stoichiometric ratio, which correlates well with the increase in mid-point pressure by formula (3). This observation is consistent with that from the AB_5 alloy series. Similar influences of stoichiometry on various properties of other two series of AB2 alloys predominated by C15 and C14/C15 phases were also reported previously (Young, et al. 2011b & 2011c).

Alloy	Full capacity (mAhg^{-1})	High-rate capacity (mAh g^{-1})	HRD	OCV at 50% DOD (V)
AB1.8	369	144	0.39	−0.859
AB1.9	369	323	0.88	−0.882
AB2.0	401	357	0.89	−0.890
AB2.1	333	308	0.92	−0.902
AB2.2	283	210	0.74	−0.915

Table 8. Summary of electrochemical properties of AB_2 alloys

5. Stoichiometry in NdMgNi-based A_2B_7 metal hydride alloys

La_2Ni_7 is an IMC with slightly lower Ni-content than $LaNi_5$ as shown in the La-Ni phase diagram (Fig. 1). ΔH of La_2Ni_7 is below the suitable range for room temperature operation as shown in Fig. 6. In order to increase ΔH, a small amount of Mg is added to replace La and brings ΔH into the suitable range for room temperature operation. So far, three MH alloys of the A_2B_7 family have been used as the negative electrode in Ni/MH rechargeable battery. Kohno et al. first introduced $La_5Mg_2Ni_{23}$ with a potential capacity of over 400 mAh g^{-1} (Kohno, et al., 2000) (Mm, Mg)(Ni, Co, Al)$_{3.3}$ alloys were used in high-capacity 2700 mAh AA-size battery by Sanyo (Yasuoka, et al., 2006) where Mm is the misch metal. Finally, (Nd, Mg)$_2$(Ni, Al)$_7$ alloys were used for the low self-discharge AA battery also introduced by Sanyo.

Five Nd_2Ni_7-based alloys with different B/A stoichiometric ratios were prepared by induction melting. The target compositions of these alloys together with the designed B/A stoichiometric ratios ranging from 3.3 to 3.7 are listed in Table 9. These alloys were annealed in 1 atm of argon at 900°C for 5 hours.

Alloy	Nd	Zr	Mg	Ni	Co	Al	B/A
AB3.3	20.3	0.2	2.7	73.1	0.1	3.5	3.3
AB3.4	19.9	0.2	2.6	73.7	0.1	3.5	3.4
AB3.5	19.4	0.2	2.6	74.1	0.1	3.5	3.5
AB3.6	19.0	0.2	2.5	74.6	0.1	3.5	3.6
AB3.7	18.6	0.2	2.5	75.0	0.1	3.6	3.7

Table 9. Designed compositions in at. % and B/A stoichiometry ratios of A_2B_7 alloys.

5.1 Influences on microstructure

The Nd-Ni phase diagram is very similar to that of La-Ni shown in Fig. 1. Under the equilibrium condition, the Nd_2Ni_7 phase has a very limited solubility. The influence of off-stoichiometry to microstructure was studied by XRD analysis, and the results are plotted in Fig. 14. Besides the reflection peaks from the Nd_2Ni_7 main phase, secondary phases of Nd, NdNi, $NdNi_2$, and $NdNi_5$ can be identified from the patterns. The lattice constants of the Nd_2Ni_7 phase were calculated and are listed in Table 10 together with the phase abundances of all observed phases. In general, as the B/A stoichiometric ratio increases, both c/a ratio

and the unit cell volume decrease as seen from the shifting in the peak into higher angle illustrated by the line shown in Fig. 14; the phase abundance of Ng_2Ni_7 remains about the same; the phase abundance of NdNi decreases; and the phase abundances of $NdNi_2$ and $NdNi_5$ increase except the last AB3.7 alloy.

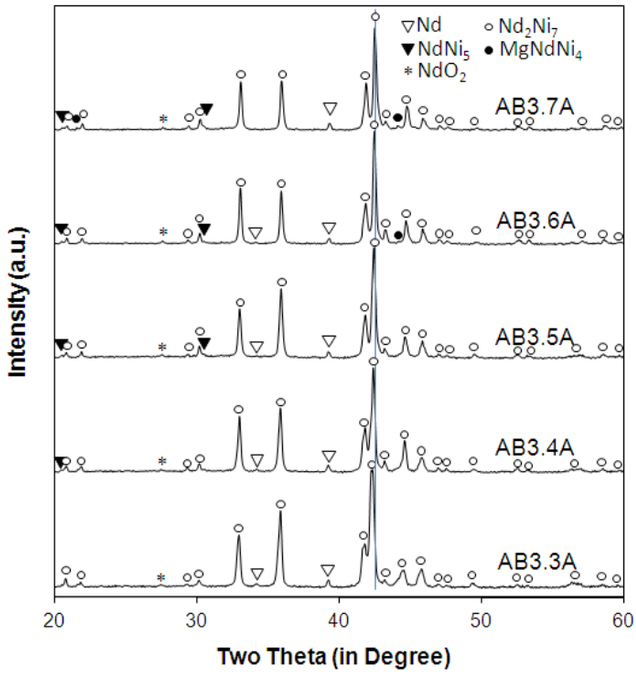

Fig. 14. XRD patterns of A_2B_7 alloys using Cu-K_α as the radiation source.

Alloy	*a* (Å)	*c* (Å)	*c*/*a*	Unit cell volume (Å^3)	Nd_2Ni_7 %	Nd %	NdNi %	$NdNi_2$ %	$NdNi_5$ %
AB3.3	5.0036	24.4325	4.883	529.7	97.6	0.9	0.5	0.4	ND
AB3.4	5.0056	24.3597	4.866	528.6	97.2	1.0	0.3	0.5	0.3
AB3.5	5.0012	24.3716	4.873	527.9	96.7	1.4	0.2	0.4	0.5
AB3.6	4.9986	24.3145	4.864	526.1	95.6	1.0	ND	1.2	1.3
AB3.7	4.9968	24.2844	4.860	525.1	95.7	1.6	ND	1.3	0.6

Table 10. Nd_2Ni_7 lattice constants and ratios, unit cell volumes, and phase abundances of Nd_2Ni_7, Nd, NdNi, $NdNi_2$, $NdNi_5$ of A_2B_7 alloys from XRD analysis.

The microstructures were further studied by SEM-EDS, and the resulting BEI micrographs are shown in Fig. 15. Five regions (identified by letters *A* to *E*) can be distinguished by backscattering contrast. The brightest spot *A* is the Nd metal. The size and abundance of Nd does not change significantly with the change in B/A stoichiometric ratio. According to EDS, region *A* has the second highest Zr-content (~ 0.3 %) next to region *E*, which is entirely composed of ZrO_2. The second brightest region, denoted by *B*, has a composition close to NdNi. The Mg-content in this region is small when compared to that of the main phase.

Region *C* is the main Nd_2Ni_7 phase and the B/A stoichiometric ratio changes from 2.91 to 3.27, 3.33, 3.33, and 3.32 as the designed B/A stoichiometric ratio increases from 3.3 to 3.4, 3.5, 3.6, and 3.7. With the incorporation of Mg in the Nd-site, the stable main phase stoichiometry is between 2.91 and 3.33. Since the extra B elements (Ni and Al) are likely to be pushed to $NdNi_5$, which is rich in B, the B/A stoichiometric ratio in the main phase is lower compared to the designed ratio. Furthermore, from the XRD analysis, the $NdNi_5$ phase can be observed in most alloys, and the amount of $NdNi_5$ phase increases with the increase in B/A stoichiometric ratio. Only the alloy with a designed B/A stoichiometry of 3.3 has too low of $NdNi_5$-content to be detected by XRD. The Mg-content in the main phase is about 3.5%, which is higher than the average Mg-content of the designed compositions. The fourth phase, region *D*, has a composition close to $NdNi_2$ with the highest Mg-content of about 12 to 15%. The SEM micrographs show appreciable amount of region *D* in all alloys. However, the XRD analysis only shows a small amount of $NdNi_2$ in the last two alloys, AB3.6 and AB3.7. The areas where the SEM micrographs were taken are usually those with the most numbers of phases and should not be used to quantify the phase abundances. Region *E*, with the darkest contrast, is from ZrO_2.

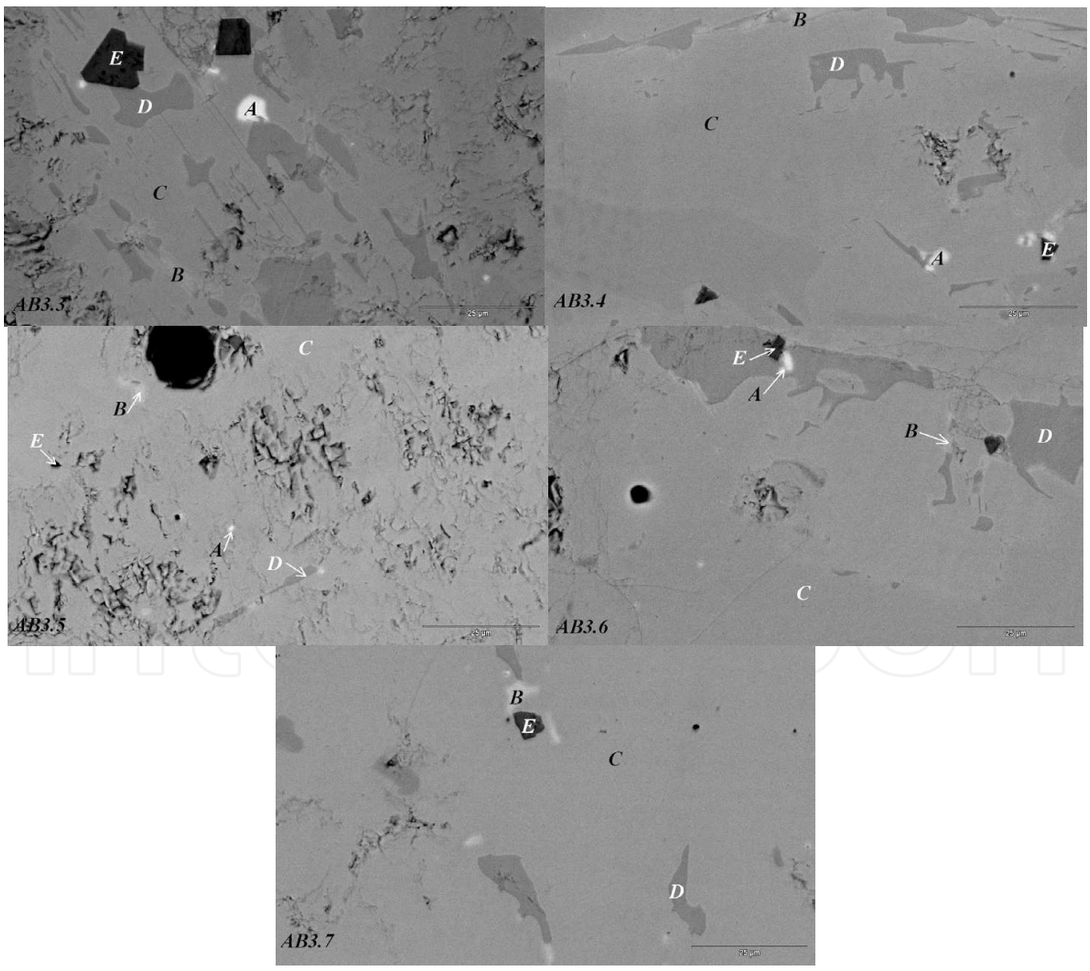

Fig. 15. SEM backscattering images for A_2B_7 alloys. Letters *A*, *B*, *C*, *D*, and *E* indicate Nd metal, NdNi, Nd_2Ni_7, $NdNi_2$, and ZrO_2, respectively.

5.2 Influences on gaseous hydrogen storage

The PCT isotherms measured at 30°C for three five A_2B_7 alloys are shown in Fig. 16 and summarized in Table 11. As the B/A stoichiometric ratio increases, the maximum hydrogen storage capacity increases in the beginning and stabilizes when the designed stoichiometry becomes ≥ 3.5; the reversible hydrogen storage capacity increases; the mid-point pressure increases by a small amount; the isotherm becomes flatter; and the hysteresis, ΔH, and ΔS remain about the same. The changes in maximum hydrogen storage capacity are similar to those in B/A stoichiometric ratio in the main Nd_2Ni_7 phase. The composition in the main phase is optimized for maximum storage capacity at B/A = 3.33. Although both the reversible capacity and the plateau pressure increase with the increase in B/A stoichiometric ratio, the increase in plateau pressure is too small to account for the large increase in reversible storage capacity. The secondary phases such as $NdNi_2$ and $NdNi_5$ are most likely to contribute to the increase in reversible hydrogen storage as the case of the ZrNi and Zr_7Ni_{10} phases in AB_2 alloy (Young, et al., 2011a). Comparing the PCT results among the AB_5, AB_2, and A_2B_7 families yields the following observations: AB_2 has the highest maximum storage capacity, AB_5 has the flattest plateau due to the smallest amount of secondary phases, and A_2B_7 has the most ordered MH structure as seen from its lowest ΔS value.

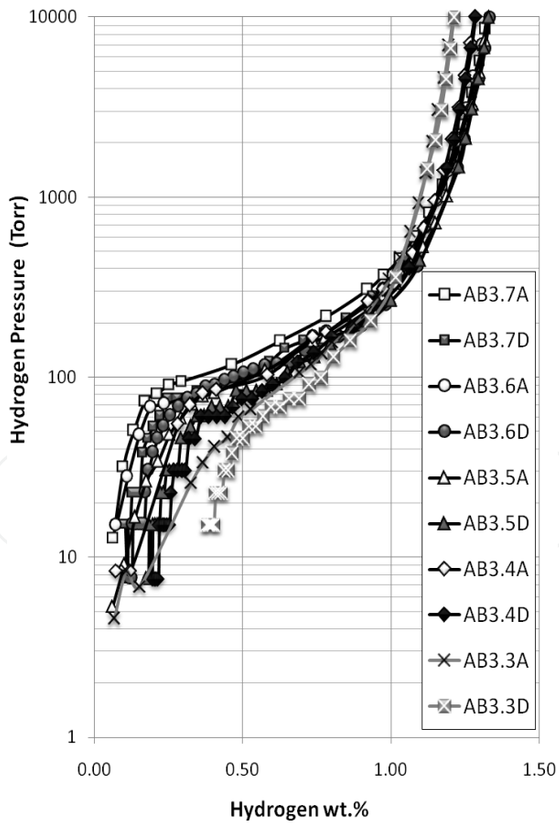

Fig. 16. PCT isotherms measured at 30°C for A_2B_7 alloys. Open and solid symbols represent data taken during absorption and desorption, respectively.

Alloy	Max. H-storage at 30°C (wt. %)	Reversible H-storage at 30°C (wt. %)	Mid-point pressure at 30°C Des. (torr)	30°C slope factor	30°C hysteresis	$-\Delta H$ (kJ mol^{-1} H_2)	$-\Delta S$ (J K^{-1} mol^{-1} H_2)
AB3.3	1.22	0.84	123	0.58	0.22	40	115
AB3.4	1.30	1.10	140	0.65	0.19	40	118
AB3.5	1.34	1.16	139	0.71	0.18	41	121
AB3.6	1.34	1.22	148	0.76	0.18	40	119
AB3.7	1.34	1.24	164	0.77	0.19	40	118

Table 11. Summary of gaseous phase hydrogen storage properties of A_2B_7 alloys.

5.3 Influences on electrochemical properties

Similar to the case of AB_5 alloys, these A_2B_7 alloys were easy to activate. All alloys reached the highest capacities within the first three cycles without any pre-treatment. The full and high-rate discharge capacities at the third cycle for each alloy are listed in Table 12. Identical to the maximum storage in gaseous phase, both the full and high-rate capacities increase and stabilize when the designed B/A becomes ≥ 3.5 due to the similar B/A stoichiometric ratio in the main Nd_2Ni_7 phase. The maximum HRD happens at alloy AB3.6. Further increase in B/A stoichiometric ratio reduces the HRD due to the reduction in $NdNi_5$ phase as indicated by the XRD analysis. OCV, measured at 50% DOD of the MH electrode against $Ni(OH)_2$/NiOOH counter electrode, shows a decrease with the increase in B/A stoichiometric ratio. According to formula (3), a higher PCT plateau pressure should generate a higher cell voltage. An increase from 123 (AB3.3) to 164 torr (AB3.7) should correspond to an increase of 0.004 volts. The voltage drop with the increase in B/A stoichiometric ratio in A_2B_7 alloys requires additional investigation.

Alloy	Full capacity (mAh g^{-1})	High-rate capacity (mAh g^{-1})	HRD	OCV at 50% DOD (V)
AB3.3	316	299	0.95	1.238
AB3.4	331	317	0.96	1.238
AB3.5	341	332	0.97	1.234
AB3.6	340	332	0.98	1.227
AB3.7	340	331	0.97	1.225

Table 12. Summary of electrochemical properties of A_2B_7 alloys.

6. Stoichiometry in MgNi-based AB metal hydride alloys

MgNi-based MH alloys have attracted much of researchers' attention due to the abundance of Mg and Ni resources. Mg metal forms a stable hydride of MgH_2 which only desorbs hydrogen at temperature above 400°C. According to the schematic of ΔH vs. Ni % in Fig. 6, a stoichiometry of Mg : Ni close to 1:1 is suitable for room temperature operation. However,

according to the Mg-Ni binary phase diagram illustrated in Fig. 17, only two IMCs are allowed at room temperature under the equilibrium condition, namely, Mg_2Ni and $MgNi_2$. The former is a MH alloy but only desorbs hydrogen at 250°C; the latter will not form any stable hydride at 1 atm. The desirable MgNi single phase (indicated by the gray arrow in Fig. 17) is not allowed. Therefore, quick quench methods under the non-equilibrium conditions, such as RF sputtering, laser ablation, and combination of melt-spin and mechanical alloying, were used to prepare the MgNi alloys for hydrogen storage and Ni/MH rechargeable battery applications.

Five thin films were prepared with the RF-sputtering technique simultaneously with a compositional gradient target, 20 mtorr Ar gas background, 200 watt of rf power in a MRC 8" multi-target system. The substrate was a Ni tab taped down to a copper plate maintained at 0°C by circulating water through the imbedded pipeline. The composition varies from Mg : Ni = 48:52 to 52:48, 57:43, 61:39, and 65:35. The deposition time was 2 hours, and the average film thickness was about 1.5 microns.

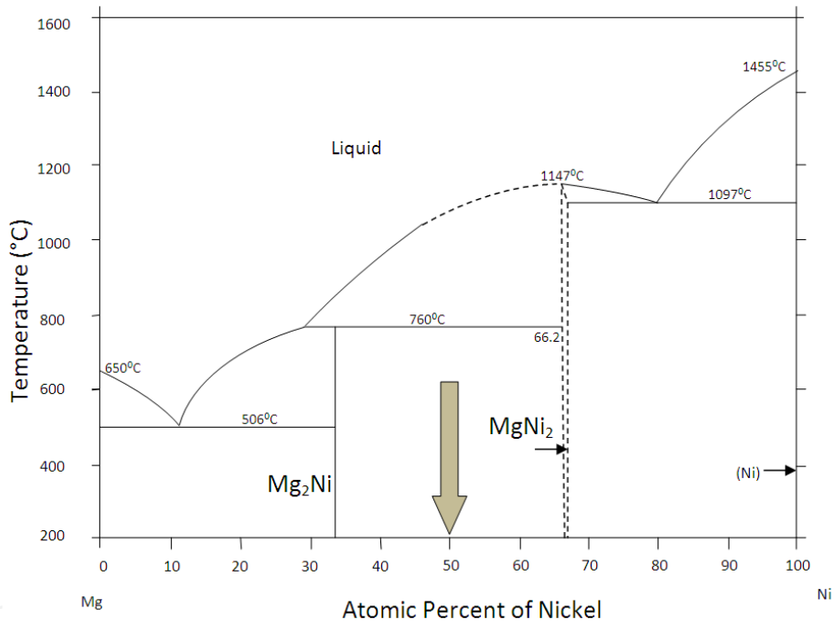

Fig. 17. Mg-Ni binary phase diagram (data from (Massalski, 1990)).

6.1 Influences on microstructure

The XRD patterns obtained from these five thin films on Ni substrate are shown in Fig. 18. The two strongest defection peaks are from the Ni-substrate. The microcrystalline phase in the film has two peaks at around 20 and 40° from the broadening of $MgNi_2$ and Mg_2Ni peaks. The positions of microcrystalline peak will not change with the film composition. While the first broad peak of microcrystalline can be seen at 20°, the second broad peak of microcrystalline (around 40°C) is unable to be discerned since it overlaps with another broad peak from the amorphous phase in the film. The center of the amorphous peak can be related to the average distance between two neighboring atoms by the Ehrenfest formula (Guinier, 1963):

$$2r\sin\theta = 1.2\lambda \quad (6)$$

where r is the average distance between two neighboring atoms and λ is the wavelength of the x-ray (in this case, 1.5418Å). The shift of the amorphous peak to the lower angle is due to the increase in the inter-atomic distance with the higher Mg (larger than Ni)-content in the thin film. As the Mg content in the alloy increases above 52%, deflection peaks from the crystalline Mg_2Ni start to appear. Film with a composition close to 1:1 ($Mg_{48}Ni_{52}$ and $Mg_{52}Ni_{48}$) shows mainly amorphous phase with smaller amounts of microcrystalline phase. With the increase in Mg-content, the Mg_2Ni crystalline phase starts to form.

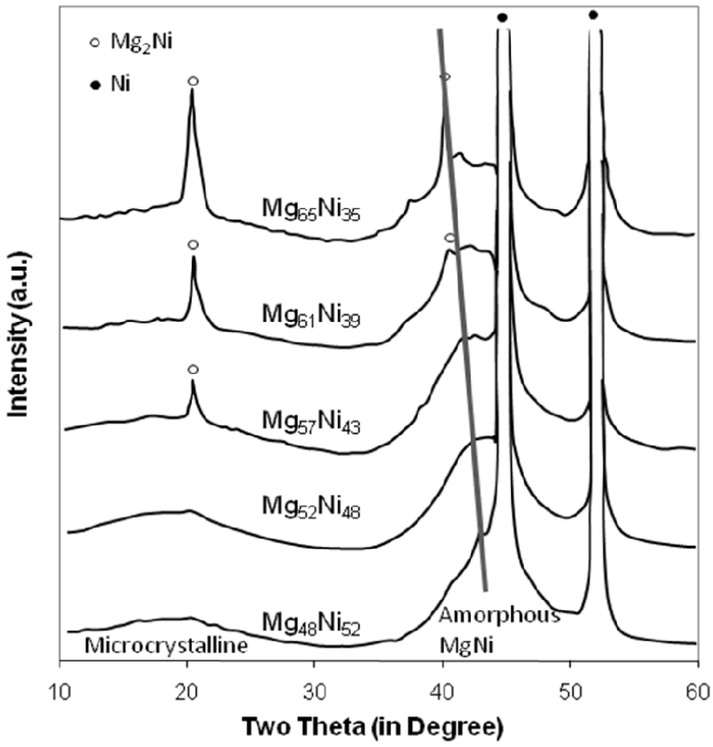

Fig. 18. XRD patterns of MgNi thin films deposited on Ni-substrate using Cu-K_α as the radiation source. The straight line illustrates the shift of amorphous peak into lower angle as the Mg-content in the film increases.

6.2 Influences on electrochemical properties

The film thickness and capacity measured at a discharged rate of 20 mA g^{-1} of each film are listed in Table 13. As the Mg-content increases, the film becomes thinner, and the discharge capacity first increases and then decreases. The maximum capacity happens at a composition of $Mg_{52}Ni_{48}$, which is mainly amorphous in nature. Both the microstructure and electrochemical capacity are strongly affected by the film composition, or in other words, stoichiometry.

Alloy composition	Film thickness (μm)	Discharge capacity (mAh g^{-1})
$Mg_{48}Ni_{52}$	2.02	302
$Mg_{52}Ni_{48}$	1.82	327
$Mg_{57}Ni_{43}$	1.64	260
$Mg_{61}Ni_{39}$	1.45	75
$Mg_{65}Ni_{35}$	1.32	20

Table 13. Summary of electrochemical properties of AB alloys.

7. Conclusion

The influences of stoichiometry on the structures, gaseous phase hydrogen storage properties, and electrochemical properties of four families of MH alloys were studied. In the cases of AB_5, AB_2, and A_2B_7, as the B/A stoichiometric ratio increases, the sizes of the unit cell of main phases decrease, resulting in less stable hydrides with higher hydrogen equilibrium pressures, the stoichiometry in the main phase increases and then becomes stabilized at the stoichiometric alloy. Further increases in the average stoichiometry increases the abundance of certain secondary phases but do not change the stoichiometry in the main phase. This suggests that the alloys under the current study have a wider composition range on the hypo-stoichiometric side (A-rich) than they do on the hyper-stoichiometric side (B-rich). The stoichiometric alloys usually have the highest gaseous phase storage capacities (both maximum and reversible). Slightly over-stoichiometric alloys are more suitable for high-power applications due to their higher HRD values. In the case of AB alloys, both the microstructure and electrochemical properties are strongly related to the film composition (stoichiometry). The optimal composition is $Mg_{52}Ni_{48}$ considering its high capacity and amorphous content.

8. References

Bendersky, L.A., Wang, K., Boettinger, W.J., Newbury, D.E., Young, K. & Chao, B. (2010). Examination of Multiphase (Zr, Ti)(V, Cr, Mn, Ni)$_2$ Ni-MH Electrode Alloys: Part II. Solid-State Transformation of the Interdendritic B2 Phase. *Metallurgical and Materials Transactions A*, Vol.41, pp.1891-1906, ISSN 1073-5623

Boettinger, W.J., Newbury, D.E., Wang, K., Bendersky, L.A., Chiu, C., Kattner, U.R., Young, K. & Chao, B. (2010). Examination of Multiphase (Zr, Ti)(V, Cr, Mn, Ni)$_2$ Ni-MH Electrode Alloys: Part I. Dendritic Solidification Structure. *Metallurgical and Materials Transactions A*, Vol.41, pp.2033-2047, ISSN 1073-5623

Chen, K.C., Allen, S.M. & Livingston, J.D. (1994). Stoichiometry and Alloying Effects on the Phase Stability and Mechanical Properties of $TiCr_2$-Base laves Phase Alloys. *High-temperature ordered intermetallic alloys VI.,* pp. 1401, MRS Symposium Proceeding Vol. 364, Material Research Society, ISBN 1-558-99265-0, Pittsburgh, Pennsylvania

De Boer, F.R., Boom, R., Mattens, W.C.M., Miedema, A.R. & Niessen, A.K. (1988). *Cohesion in Metal*, pp. 4, North-Holland, ISBN 0-444-87098-9, Amsterdam

Guinier, A. (1963). *X-ray Diffraction in Crystals, Imperfect Crystals and Amorphous Bodies*, pp.73, Freeman, ISBN 0-486-68011-8, San Francisco

Kodama, T., Anada, H. & Kaminaka, H. (1995). The Site Occupancies for the Excess Manganese Atoms and the Third Element Niobium in the Intermetallic Compound $ZrMn_2$. *Journal of Alloys and Compounds*, Vol. 224, pp.70-75, ISSN 0925-8388

Kohno, T., Yoshida, H., Kawashima, F., Inaba, T., Sakai, I., Yamamoto, M. & Kanda, M. (2000). Hydrogen Storage Properties of New Ternary System Alloys: La_2MgNi_9, $La_5Mg_2Ni_{23}$, La_3MgNi_{14}. *Journal of Alloys and Compounds*, Vol.311, pp.L5-L7 , ISSN 0925-8388

Massalski, T.B. (1990). *Binary Alloy Phase Diagram*, ASM International, ISBN 0-87170-403-X, Ohio, USA.

Osumi, Y., Suzuki, H., Kato, A., Oguro, K., Kawai, S. & Kaneko, M. (1983). Hydrogen Absorption-desorption Charateristics of Mm-Ni-Al-M and Mm-Ni-Mn-M Alloys (Mm = misch metal). *Journal of Less-common Metals*, Vol.89, pp.287-292 , ISSN 0022-5088

Pauling, L. (1987). Factors Determining the Average Atomic Volumes in Intermetallic Compounds. *Proceedings of the National Academy of Science of the United State of America*, Vol.84, pp.4754-4756, ISSN 002708424

Shaltiel, D., Jacob, I. & Davidov, D. (1977). Hydrogen Absorption and Desorption Properties of AB_2 Laves-phase Pseudobinary Compounds. *Journal of Less-common Metals*, Vol.53, pp.117-131, ISSN 0022-5088

Thoma, D.J. & Perepezko, J.H. (1995). A Geometric Analysis of Solubility Ranges in Laves Phases. *Journal of Alloys and Compounds*, Vol.224, pp.330-341, ISSN 0925-8388

Yasuoka, S., Magari, Y., Murata, T., Tanaka, T., Ishida, J., Nakamura, H., Nohma, T., Kahara, M., Baba, Y. & Teraoka, H. (2006). Development of High-capacity Nickel-metal Hydride Batteries Using Superlattice Hydrogen-absorbing Alloys. *Journal of Power Sources*, Vol.156, pp.662-666, ISSN 0378-7753

Young, K., Fetcenko, M.A., Ouchi, T., Li, F., & Koch, J. (2008). Structural, Thermodynamic, and electrochemical Properties of $Ti_xZr_{1-x}(VNiCrMnCoAl)_2$ C14 Laves Phase Alloys. *Journal of Alloys and Compounds*, Vol.464, pp.238-247, ISSN 0925-8388

Young, K., Ouchi, T., Koch, J. & Fetcenko, M.A. (2009a). The Role of Mn in C14 Laves Phase Multi-component Alloys for NiMH Battery Application. *Journal of Alloys and Compounds*, Vol. 477, pp.749-758 , ISSN 0925-8388

Young, Y., Ouchi, T. & Fetcenko, M.A. (2009b). Pressure-composition-temperature Hysteresis in C14 Laves Alloys: Part 1. Simple Ternary Alloys. *Journal of Alloys and Compounds*, Vol.480, pp.428-433, ISSN 0925-8388

Young, K., Huang, B., Regmi, R.K., Lawes, G. & Liu, Y. (2010a). Comparisons of Metallic Clusters Imbedded in the Surface Oxide of AB_2, AB_5, and A_2B_7 Alloys. *Journal of Alloys and Compounds*, Vol.506, pp.831-840, ISSN 0925-8388

Young, K., Ouchi, T., Huang, B., Chao, B., Fetcenko, M.A., Bendersky, L.A., Wang, K. & Chiu, C. (2010b). The Correlation of C14/C15 Phase Abundance and Electrochemical Properties in the AB_2 Alloys. *Journal of Alloys and Compounds*, Vol.506, pp.841-848, ISSN 0925-8388

Young, K., Regmi, R., Lawes, G., Ouchi, T., Reichman, B., Fetcenko, M.A. & Wu, A. (2010c). Effects of Aluminum Substitution in C14-rich Multi-component Alloys for NiMH Battery Application. *Journal of Alloys and Compounds*, Vol.490, pp.282-292, ISSN 0925-8388

Young, K., Nei, J., Ouchi, T. & Fetcenko, M.A. (2011a). Phase Abundances in AB_2 Metal Hydride Alloys and Their Correlations to Various Properties. *Journal of Alloys and Compounds*, Vol.509, pp.2277-2284 , ISSN 0925-8388

Young, K., Ouchi, T., Yang, J. & Fetcenko, M.A. (2011b) Studies of off-Stoichiometric AB_2 Metal Hydride Alloy: Part 1. Structural Characteristics. *International Journal of Hydrogen Energy*, Vol.36, pp.11137-11145, ISSN 0360-3199

Young, K., Ouchi, T., Yang, J. & Fetcenko, M.A. (2011c) Studies of off-Stoichiometric AB_2 Metal Hydride Alloy: Part 2. Hydrogen Storage and Electrochemical Properties. *International Journal of Hydrogen Energy*, Vol.36, pp.11146-11154, ISSN 0360-3199

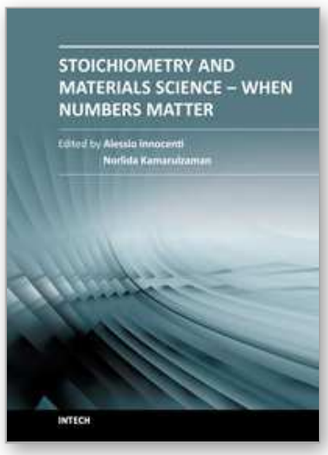

Stoichiometry and Materials Science - When Numbers Matter

Edited by Dr. Alessio Innocenti

ISBN 978-953-51-0512-1
Hard cover, 436 pages
Publisher InTech
Published online 11, April, 2012
Published in print edition April, 2012

The aim of this book is to provide an overview on the importance of stoichiometry in the materials science field. It presents a collection of selected research articles and reviews providing up-to-date information related to stoichiometry at various levels. Being materials science an interdisciplinary area, the book has been divided in multiple sections, each for a specific field of applications. The first two sections introduce the role of stoichiometry in nanotechnology and defect chemistry, providing examples of state-of-the-art technologies. Section three and four are focused on intermetallic compounds and metal oxides. Section five describes the importance of stoichiometry in electrochemical applications. In section six new strategies for solid phase synthesis are reported, while a cross sectional approach to the influence of stoichiometry in energy production is the topic of the last section. Though specifically addressed to readers with a background in physical science, I believe this book will be of interest to researchers working in materials science, engineering and technology.

InTech Europe
University Campus STeP Ri
Slavka Krautzeka 83/A
51000 Rijeka, Croatia
Phone: +385 (51) 770 447
Fax: +385 (51) 686 166
www.intechopen.com

InTech China
Unit 405, Office Block, Hotel Equatorial Shanghai
No.65, Yan An Road (West), Shanghai, 200040, China
中国上海市延安西路65号上海国际贵都大饭店办公楼405单元
Phone: +86-21-62489820
Fax: +86-21-62489821

IntechOpen